Hybrid models of reactive transport in porous and fractured media

Ilenia Battiato [a], Daniel M. Tartakovsky [a,*], Alexandre M. Tartakovsky [b], T.D. Scheibe [b]

[a] Department of Mechanical and Aerospace Engineering, University of California, San Diego, 9500 Gilman Drive, La Jolla, CA 92093, USA
[b] Pacific Northwest National Laboratory, P.O. Box 999, Richland, WA 99352, USA

ARTICLE INFO

ABSTRACT

Darcy-scale models of flow and transport in porous media often fail to describe experimentally observed phenomena, while their pore-scale counterparts are accurate but can be computationally prohibitive. Most numerical multiscale models, which seek to combine these two descriptions, require empirical closures and/or assumptions about the behavior of pore-scale quantities at the continuum (Darcy) scale. We present a general formulation of an iterative hybrid numerical method that links the pore and continuum scales without resorting to such approximations. The algorithm treats the fluxes exchanged at the internal boundaries between pore- and continuum-scale domains as unknown, and allows for iteratively determined boundary conditions to be applied at the pore-scale in order to guarantee flux continuity. While the algorithm proposed is general, we use it to model transport in a fracture with chemically reactive walls. Results demonstrate significant improvement upon standard continuum-scale formulations.

© 2011 Elsevier Ltd. All rights reserved.

1. Introduction

Standard continuum (Darcy-scale) models of flow and transport in porous media (e.g., Darcy's law for single- and multi-phase flows, and an advection–dispersion equation or ADE for transport) often fail to describe experimentally observed phenomena, including the extent of reactions in mixing-controlled chemical transformations [12,24], asymmetrical long tails of breakthrough curves [17], and the onset of instability in variable density flows [21]. Such failures occur when approximations and closure assumptions underpinning these models break down [4–6]. These approximations and assumptions are needed to transition from "first-principle" models that are valid at the pore scale (e.g., the Stokes equations for flow and advection–diffusion equations for transport) to their largely phenomenological counterparts defined at a continuum scale (e.g., Darcy's law and ADE).

While pore-scale simulations — employing alternatively lattice Boltzmann methods [20], the smoothed particle hydrodynamics (SPH) method [15], or direct numerical simulations [18], among other computational techniques [15] — can obviate the need for these approximations, they are impractical as a predictive tool due to both high computational costs and the lack of detailed information about pore geometry of natural porous media larger than a small core. The search for ways to combine the physical rigor of pore-scale modeling with the computational efficiency of its continuum-scale counterpart has motivated the development of hybrid pore-scale/continuum-scale algorithms, e.g., [14,22].

Hybrid simulations, also known as a multi-algorithm approach or algorithm refinement, provide significant computational speed-up when a sub-domain Ω_p wherein pore-scale simulations are required (i.e., wherein continuum models become invalid) is much smaller than a total computational domain Ω. The inequality [1,2],

$$\frac{\|\Omega_{pc}\|}{\|\Omega\| - \|\Omega_p\|}\frac{C_{pc}}{C_p} \ll 1$$

provides a more precise formulation of this statement. Here $\|\Omega\|$, $\|\Omega_p\|$, and $\|\Omega_{pc}\|$ are the respective volumes of Ω, Ω_p, and a "handshake" region Ω_{pc} wherein both continuum and pore-scale simulations are coupled; and C_p and C_{pc} are the computational costs per unit volume for pore-scale and coupling simulations, respectively. This condition takes advantage of the fact that the computational cost of continuum-scale simulations is much smaller than that of pore-scale simulations (C_p). As pointed out in [1], a hybrid algorithm is beneficial "even if the algorithmic interface is computationally more expensive than either algorithm, as long as the interface region and the region using the more expensive method are each small fractions of the total volume." The latter condition is satisfied in highly localized flow and transport phenomena, such as flow and transport to/from point sources and propagation of reactive fronts. Tools for identifying the regions Ω_p, wherein continuum models break down, were developed in [5,6].

It is important to distinguish hybrid algorithms from multiscale numerical approaches that are based on empirical closures [9], upscaling methods [13] and/or assumed macroscopic behavior of microscopic variables [7]. Multiscale algorithms employ "effective" representations of pore-scale processes, which share many approximations and assumptions with continuum models. For example,

the multiscale methods based on upscaling techniques [9,13] impose periodic boundary conditions on a pore-scale problem, rely on truncated Taylor expansions of pore-scale variables, and/or employ empirical closures.

We present a hybrid algorithm that couples pore-scale simulations in a small domain Ω_p with continuum simulations elsewhere in the computational domain, Ω/Ω_p. The coupling is accomplished via an iterative procedure in a handshake region Ω_{pc}, where both the pore-scale and continuum-scale descriptions are solved iteratively to ensure the continuity of state variables and their fluxes across the interface between Ω_p and the rest of the computational domain.

The manuscript is organized as follows. Section 2 contains a general formulation of flow and transport equations at the pore (Section 2.1) and continuum (Section 2.2) scales, as well as an outline of the proposed hybrid algorithm (Section 2.3). Both the hybrid formulation and its numerical implementation are made concrete in Section 3 by applying them to model Taylor dispersion in a planar fracture with chemically reactive walls. In Section 4, we use this well-studied problem to validate our hybrid algorithm via comparison with analytical solutions and two-dimensional pore-scale numerical simulations.

2. Hybrid formulation of flow and transport in porous media

2.1. Governing equations at the pore scale

Consider reactive transport in a fully-saturated porous medium Ω^T. Within the pore space Ω_p^T contained in Ω^T, single-phase flow of an incompressible fluid is described by the Stokes and continuity equations,

$$\mu\nabla^2\mathbf{v} - \nabla p = \mathbf{0}, \quad \nabla \cdot \mathbf{v} = 0, \tag{1}$$

where $\mathbf{v}(\mathbf{x})$, $p(\mathbf{x})$ and μ are the fluid's velocity, dynamic pressure, and dynamic viscosity, respectively. Flow equations (1) are subject to the no-slip boundary condition on the solid–liquid interface $\Gamma_{s\ell}^T$, which is taken to be impermeable to flow, i.e., $\mathbf{v} = \mathbf{0}$ for $\mathbf{x} \in \Gamma_{s\ell}^T$. The flow is driven by boundary conditions imposed on $\partial\Omega^T$, the external boundary of Ω^T.

The fluid contains a dissolved species with molar concentration $c(\mathbf{x},t)$ [M L^{-3}] that undergoes advection, molecular diffusion and a linear heterogeneous reaction at the solid–liquid interface $\Gamma_{s\ell}^T$. The evolution of $c(\mathbf{x},t)$ is described by an advection–diffusion equation,

$$\frac{\partial c}{\partial t} + \nabla \cdot (\mathbf{v}c) = \mathscr{D}\nabla^2 c, \tag{2a}$$

subject to the boundary condition on the solid–fluid interface $\Gamma_{s\ell}^T$,

$$-\mathbf{n} \cdot \mathscr{D}\nabla c = \mathscr{K}c, \tag{2b}$$

and boundary conditions on $\partial\Omega^T$. Here $\mathscr{D}$ [$L^2 T^{-1}$] is the molecular diffusion coefficient, $\mathscr{K}(\mathbf{x})$ [$L\,T^{-1}$] is the reaction rate constant for a surface reaction (e.g., linear microbial degradation), and $\mathbf{n}(\mathbf{x})$ is the outward unit normal vector of $\Gamma_{s\ell}^T$.

2.2. Governing equations at the continuum scale

Let $\overline{A}(\mathbf{x},t)$ denote the volumetric average of a pore-scale quantity $A(\mathbf{x},t)$ defined as

$$\overline{A}(\mathbf{x},t) \equiv \frac{1}{\phi\|\mathscr{V}\|}\int_{\mathscr{V}(\mathbf{x})} A(\mathbf{y},t)\mathrm{d}\mathbf{y}, \tag{3}$$

where $\phi(\mathbf{x})$ is the porosity of a porous medium, and the averaging volume $\mathscr{V}$ might or might not constitute a representative elemen-

tary volume (REV). Averaging (1), i.e., upscaling the flow equations from the pore scale to the continuum scale, leads to Darcy's law [4],

$$\mathbf{V} = -\frac{\mathbf{k}}{\mu}\nabla\bar{p}, \tag{4}$$

where $\mathbf{k}(\mathbf{x})$ is the permeability of the porous medium, and $\mathbf{V}(\mathbf{x}) = \phi\bar{\mathbf{v}}$ is Darcy's flux. The validity of (4) requires that the Reynolds number Re$_c$ satisfy the inequality [8, p.74, and the references therein]

$$\text{Re}_c \equiv \frac{|\mathbf{V}|d}{v} < 10, \tag{5}$$

where d is a typical length associated with grain geometry, and v is the fluid's kinematic viscosity.

A continuum-scale formulation of the pore-scale transport problem (2) typically used in practice is

$$\phi\frac{\partial\bar{c}}{\partial t} + \phi\nabla \cdot (\mathbf{V}c) = \nabla \cdot (\mathbf{D}\nabla\bar{c}) - K\bar{c}, \tag{6}$$

where $\mathbf{D}(\mathbf{x})$ is the dispersion tensor, and $K(\mathbf{x})$ is the effective reaction rate. Eq. (6) can be derived by standard upscaling methodologies, such as multiple-scale expansions or volumetric averaging [5, and references therein]. Regardless of the choice of an upscaling technique, a number of simplifying approximations are required for (6) to be valid [5,6]. These can be summarized by the phase diagram developed in [5] and reproduced in Section 3 for completeness.

2.3. General hybrid formulation

We are concerned with transport regimes in which Re$_c$ < 10, i.e., the Darcy law (4) is valid over the whole computational domain Ω^T but one or more of the sufficient conditions [5,6] for the validity of the continuum-scale transport Eq. (6) break down in a sub-domain Ω_p of the computational domain Ω^T, (Fig. 1). In Ω_p, the averaging of (2) results in an integro-differential equation

$$\phi\frac{\partial\bar{c}}{\partial t} + \overline{\nabla \cdot (\mathbf{v}c)} = \mathscr{D}\overline{\nabla^2 c}, \tag{7}$$

where the averaging (3) is now defined over $\mathscr{V} \equiv \Omega_p(\mathbf{x}^\star)$ and $\mathbf{x}^\star$ is the centroid of Ω_p, i.e., the sub-domain Ω_p shrinks to a point $\mathbf{x}^\star \in \Omega^T$. Violation of some of the sufficient conditions [5,6] prevents the averaging integrals in (7) from being converted into the corresponding terms for the macroscopic (average) concentration $\bar{c}$ in (6).

According to Gauss' theorem, (7) can be rewritten as

$$\phi\frac{\partial\bar{c}}{\partial t} = \frac{1}{\phi\|\Omega_p\|}\int_{\Gamma_p} \mathbf{n} \cdot (\mathscr{D}\nabla c - \mathbf{v}c)\mathrm{d}s, \tag{8}$$

where Γ_p is the bounding surface of Ω_p, and $\mathrm{d}s$ is an infinitesimal element of Γ_p. Since the surface $\Gamma_p = \Gamma_{\ell\ell}^p \cup \Gamma_{s\ell}^p$ consists of liquid–liquid ($\Gamma_{\ell\ell}^p$) and solid–liquid ($\Gamma_{s\ell}^p$) segments, boundary condition (2b) and the no-slip condition yield
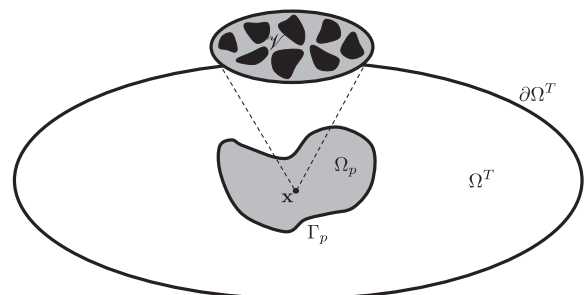

Fig. 1. A schematic representation of the pore- and continuum-scale domains.

$$\phi \frac{\partial \bar{c}}{\partial t} = -\frac{1}{\phi \|\Omega_p\|} \int_{\Gamma_{\ell\ell}^p} q_n \mathrm{d}s - \frac{1}{\phi \|\Omega_p\|} \int_{\Gamma_{s\ell}^p} \mathscr{K} c \mathrm{d}s, \qquad (9)$$

where $q_n(\mathbf{x},t) = \mathbf{n} \cdot (\mathbf{v}c - \mathscr{D}\nabla c)$ is the pore-scale mass flux (or flux density) through the liquid–liquid portion of the boundary, Γ_p. The right-hand-side of (9) depends on the pore-scale quantities. It represents the fluxes exchanged at the boundary Γ_p between the pore- and continuum-scale descriptions. Multiscale approaches [7,9,13, among others] decouple the two descriptions by employing closure assumptions to express the unresolved pore-scale flux $q_n(\mathbf{x},t)$ in terms of its continuum-scale counterpart. A typical strategy is to represent the pore-scale concentration $c = \bar{c} + c'$ as the sum of its average $\bar{c}$ and corresponding fluctuations c', to linearize $f(c) = f(\bar{c}) + c'(\mathrm{d}f/\mathrm{d}c)|_{c=\bar{c}} + \cdots$, to postu-

late a numerical or analytical closure for c', and to impose boundary conditions on Γ_p (the most common being a periodic condition).

In contrast, our goal is to compute the unresolved pore-scale flux q_n without any assumption on the pore-scale behavior and without resorting to linearization of the general reactive term $f(c)$ when the latter is present. To this end, we obtain the pore-scale concentration $c(\mathbf{x},t)$ in (9) by solving the transport problem (2) defined on Ω_p. The boundary condition (2b) is now defined on the union of all solid–liquid surfaces $\Gamma_{s\ell}$ contained in Ω_p. On the fluid–fluid segments $\Gamma_{\ell\ell}^p$, mass conservation requires that $\mathbf{n} \cdot (\mathscr{D}\nabla c - \mathbf{v}c) = q_n$. The pore-scale flux $q_n(\mathbf{x},t)$, which represents a boundary condition for the pore-scale problem (2) and a source term for the continuum-scale Eq. (9), is unknown.
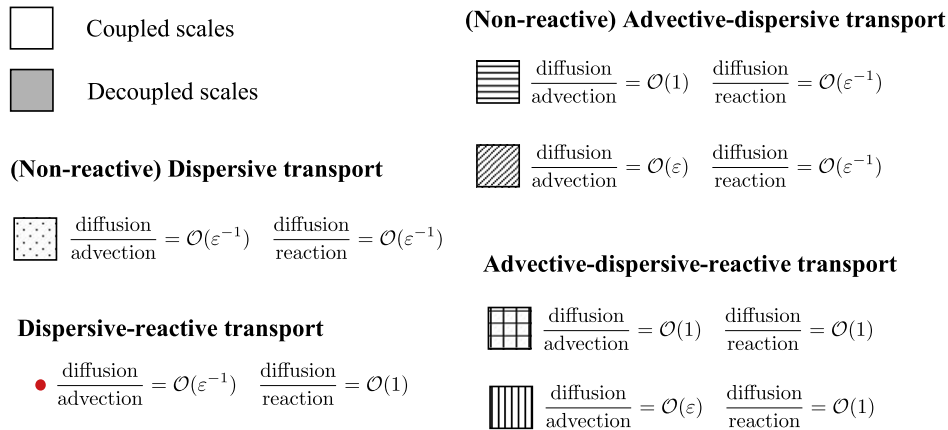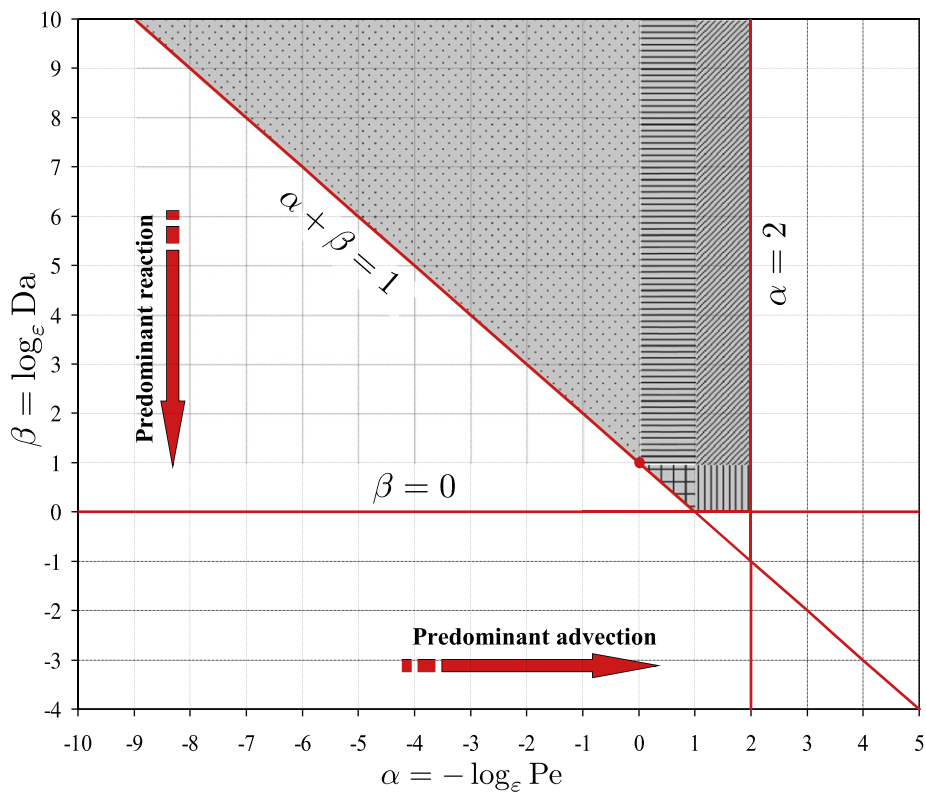

Fig. 2. Phase diagram indicating the range of applicability of macroscopic advection–reaction–diffusion equations in terms of the Péclet (Pe) and Damköhler (Da) numbers. The grey region identifies the sufficient conditions under which the macroscopic equations hold. In the white region, macro- and micro-scale problems are coupled and have to be solved simultaneously. Also identified are different transport regimes depending on the order of magnitude of Pe and Da. Diffusion, advection, and reaction are of the same order of magnitude at the point $(\alpha, \beta) = (1, 0)$. Reproduced from [5].

In summary, the hybrid pore-scale/continuum-scale algorithm contains the three unknowns $(c, \bar{c}, q_n)$ that satisfy a system of coupled partial-differential equations,

$$\phi \frac{\partial \bar{c}}{\partial t} + \phi \nabla \cdot (\mathbf{V}\bar{c}) = \nabla \cdot (\mathbf{D}\nabla\bar{c}) - K\bar{c}, \quad \mathbf{x} \in \Omega^T, \quad t > 0, \tag{10}$$

$$\phi \frac{\partial \bar{c}}{\partial t} = \frac{1}{\phi\|\Omega_p\|} \int_{\Gamma_{\ell\ell}} q_n \mathrm{d}\mathbf{x} - \frac{1}{\phi\|\Omega_p\|} \int_{\Gamma_{s\ell}} \mathscr{K} c \mathrm{d}\mathbf{x}, \quad \mathbf{x} = \mathbf{x}^\star, \quad t > 0, \tag{11}$$

$$\frac{\partial c}{\partial t} + \nabla \cdot (\mathbf{v}c) = \mathscr{D}\nabla^2 c, \quad \mathbf{x} \in \Omega_p, \quad t > 0, \tag{12}$$

$$\mathbf{n} \cdot (\mathscr{D}\nabla c - \mathbf{v}c) = q_n, \quad \mathbf{x} \in \Gamma_{\ell\ell}, \quad t > 0, \tag{13}$$

$$-\mathbf{n} \cdot \mathscr{D}\nabla c = \mathscr{K}c, \quad \mathbf{x} \in \Gamma_{s\ell}, \quad t > 0, \tag{14}$$

supplemented by initial conditions and boundary conditions on the external domain $\partial\Omega^T$.

In the following section we apply this hybrid algorithm to model transport in a fracture with chemically reactive walls.

3. Transport in a fracture with reactive walls

Consider transport of a reactive solute by advection and diffusion in a fracture of width $2H$. The solute undergoes a first-order heterogeneous reaction at the walls of the channel. The flow domain $\Omega = \{(x,y) : x \in (0,\infty), |y| < H\}$ has the boundary $\Gamma = \{(x,y) : x \in (0,\infty), |y| = H\}$.

Assuming laminar, fully developed flow inside the fracture, the "pore-scale" velocity in (1) is given by Poiseuille's law, $\mathbf{V} = (u,0)^T$, where

$$u(y) = u_m\left[1 - \left(\frac{y}{H}\right)^2\right] \tag{15}$$

and u_m is the maximum velocity at the center of the fracture ($y = 0$). The general pore-scale transport problem (2) reduces to

$$\frac{\partial c}{\partial t} + u(y)\frac{\partial c}{\partial x} - \mathscr{D}\left(\frac{\partial^2 c}{\partial x^2} + \frac{\partial^2 c}{\partial y^2}\right) = 0, \quad (x,y) \in \Omega, \quad t > 0, \tag{16a}$$

$$-\mathscr{D}\frac{\partial c}{\partial y} = \mathscr{K}c, \quad (x,y) \in \Gamma, \quad t > 0. \tag{16b}$$

The average concentration $\bar{c}(x,t)$ in (3) is now defined as

$$\bar{c}(x,t) \equiv \frac{1}{2H}\int_{-H}^{H} c(x,y,t)\mathrm{d}y. \tag{17}$$

It satisfies a version of the continuum (Darcy-scale) transport Eq. (6) that has the form [16]

$$\frac{\partial \bar{c}}{\partial t} + U\frac{\partial \bar{c}}{\partial x} + K\bar{c} = D\frac{\partial^2 \bar{c}}{\partial x^2}, \quad x \in (0,\infty), \quad t > 0, \tag{18a}$$

where

$$U = u_m\left(\frac{2}{3} + \frac{4\mathrm{Da}_y}{45}\right), \quad K = \frac{\mathscr{K}}{H}\left(1 - \frac{\mathrm{Da}_y}{3}\right), \quad D = \mathscr{D}\left(1 + \frac{8\mathrm{Pe}_y^2}{945}\right) \tag{18b}$$

and

$$\mathrm{Pe}_y = \frac{u_m H}{\mathscr{D}}, \quad \mathrm{Da}_y = \frac{\mathscr{K}H}{\mathscr{D}}. \tag{18c}$$

The validity of (18) requires that L, a macroscopic characteristic length scale in the x direction, be much larger than H, i.e., $\epsilon = H/L \ll 1$; and places a number of constraints on the order of magnitude of the Péclet (Pe_y) and Damköhler (Da_y) numbers (Fig. 2).

Our focus is on transport regimes wherein one or more of these constraints are violated in a small portion of the computational domain, $\Omega_p = \{(x,y): x \in (a,b), |y| < H\}$. Eq. (18) is valid in the rest of the computational domain. To simplify the presentation, we

assume that Ω_p corresponds to a single macroscale grid block. Then the domain of pore-scale simulations Ω_p and the handshake domain Ω_{pc} coincide. Domains Ω_p that are larger than a single grid block can be easily handled by following a procedure similar to that described below. Possible effects on numerical robustness are discussed in [9, p. 511].

Since (18) is no longer valid in Ω_p, we employ its nonlocal counterpart (9), which for the problem under consideration takes the form

$$\frac{\partial \bar{c}}{\partial t} = \mathscr{D}\frac{\partial^2 \bar{c}}{\partial x^2} - \frac{\mathscr{K}J_c}{2H} - \overline{u(y)\frac{\partial c}{\partial x}}, \quad (x,y) \in \Omega_p \tag{19}$$

where $J_c = c(x,H) + c(x,-H)$ and the pore-scale concentration $c(x,y,t)$ satisfies (16). Eq. (19) is supplemented by the boundary conditions at the internal boundary $\Gamma_p = \{(x,y) : x = a,b; y \in (-H,H)\}$,

$$\mathbf{n} \cdot (\mathbf{V}c - \mathscr{D}\nabla c) = q_n. \tag{20}$$

The following sections contain a finite-volume discretization of the averaged equations (18) and (19). A finite-volume discretization of the pore-scale equations (16) is standard [23] and not reproduced here explicitly.

3.1. Finite-volume formulation

We discretize the macroscopic space–time domain into N_X and N_T intervals of width ΔX_I and ΔT, respectively (Fig. 3). Spatial nodes of the macroscopic domain, Ω/Ω_p, are defined as

$$X_{I+1} = X_I + (\Delta X_I + \Delta X_{I+1})/2, \quad I = 1,\ldots,N_X \tag{21}$$

and their temporal counterparts are defined as

$$T_N = N\Delta T, \quad N = 0, 1, \ldots, N_T. \tag{22}$$

The western and eastern boundaries of the control volume (CV) centered at X_I are given by $X_{I-1/2} = X_I - \Delta X_I/2$ and $X_{I+1/2} = X_I + \Delta X_I/2$, respectively. The distance between two adjacent nodes is $\Delta X_{I+1/2} = X_{I+1} - X_I$. The western and eastern boundaries of the computational domain coincide with the western and eastern boundaries of the first and last CVs, $X_{1/2}$ and $X_{N_X+1/2}$, respectively.

Let $I^\star$ denote the index of the CV in which the standard macroscopic Eq. (18) breaks down. In this formulation, the single $I^\star$-th CV represents both the domain of pore-scale simulations Ω_p and the handshake region Ω_{pc}. Instead of (18), both its nonlocal counterpart (19) and the pore-scale transport equation (16) have to be solved in the $I^\star$-th CV. In the rest of the computational domain, (18) is valid. The $I^\star$-th CV is discretized into n_x and n_y intervals of width Δx_i and Δy_j in the x and y directions, respectively. Spatial nodes (x_i, y_i) of the microscopic domain Ω_p (the $I^\star$-th CV) are defined as

$$x_{i+1} = x_i + (\Delta x_i + \Delta x_{i+1})/2, \quad i = 1,\ldots,n_x, \tag{23a}$$

$$y_{j+1} = y_j + (\Delta y_j + \Delta y_{j+1})/2, \quad j = 1,\ldots,n_y. \tag{23b}$$

The four surfaces bounding a CV centered at (x_i, y_j) are at locations $x_{i-1/2} = x_i - \Delta x_i/2$ (west), $x_{i+1/2} = x_i + \Delta x_i/2$ (east), $y_{j-1/2} = y_j - \Delta y_j/2$ (south), and $y_{j+1/2} = y_j + \Delta y_j/2$ (north). The distances between two adjacent nodes in the x and y directions are $\Delta x_{i+1/2} = x_{i+1} - x_i$ and $\Delta y_{j+1/2} = y_{j+1} - y_j$, respectively. The western and eastern boundaries of Ω_p coincide with the western and eastern boundaries of the $I^\star$-th
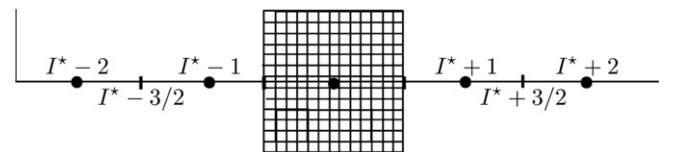

Fig. 3. A finite-volume discretization of the computational domain for a hybrid 1D/2D formulation.

macroscopic CV, $X_{I^\star-1/2}$ and $X_{I^\star+1/2}$, respectively (Fig. 3). Time t in the pore-scale simulations is discretized into n_t intervals of width Δt, such that $\Delta T = n_t \Delta t$ and $t_n = n\Delta t$ with $n = 0, 1, \ldots$.

Let us define $\bar{c}_I^N = \bar{c}(X_I, T_N)$ and $c_{i,j}^n = c(x_i, y_j, t_n)$. In Appendix A.1 we derive a finite-volume fully-implicit approximation of the macroscopic Eqs. (18) and (19),

$$A_{I-1}\bar{c}_{I-1}^{N+1} + A_I\bar{c}_I^{N+1} + A_{I+1}\bar{c}_{I+1}^{N+1} = \text{RHS}_I^N, \tag{24}$$

where, for nodes $I = \{1, \ldots, I^\star - 1\} \cup \{I^\star + 1, \ldots, N_X\}$,

$$A_{I-1} = -a_{I-1}, \quad A_I = \frac{\Delta X_I}{\Delta T} + \bar{a}_I, \quad A_{I+1} = -a_{I+1}, \quad a_0 = 0, \tag{25a}$$

$$a_{I+1} = \max\left(-U, \mathcal{D}_{I+1/2} - \frac{U}{2}, 0\right), \quad \mathcal{D}_{I+1/2} = \frac{D}{\Delta X_{I+1/2}}, \tag{25b}$$

$$a_{I-1} = \max\left(-U, \mathcal{D}_{I-1/2} + \frac{U}{2}, 0\right), \quad \mathcal{D}_{I-1/2} = \frac{D}{\Delta X_{I-1/2}}, \tag{25c}$$

$$a_{N_X} = 0, \quad \bar{a}_I = a_{I-1} + a_{I+1} + K\Delta X_I - \bar{S}_I, \tag{25d}$$

$$\text{RHS}_I^N = \frac{\Delta X_I}{\Delta T}\bar{c}_I^N + \widetilde{S}_I, \tag{25e}$$

and $\widetilde{S}_I$ and $\bar{S}_I$ represent a numerical discretization of external boundary conditions at the macroscale.

At node $I^\star$, the coefficients in (24) take the form (Appendix A.2)

$$A_{I^\star-1} = -d_{I^\star-1/2}, \quad A_I^\star = \frac{\Delta X_{I^\star}}{\Delta T} + d_{I^\star-1/2} + d_{I^\star+1/2}, \quad A_{I^\star+1} = -d_{I^\star+1/2}, \tag{26a}$$

$$\text{RHS}_{I^\star}^N = \frac{\Delta X_{I^\star}}{\Delta T}\bar{c}_{I^\star}^N + \frac{1}{2HN_T}\sum_{k=1}^{n_t} G^{k+1}, \tag{26b}$$

with

$$G^k = -\mathscr{K}\sum_{i=1}^{n_x}\Delta x_i(c_{i,H}^k + c_{i,-H}^k) - \begin{cases} \int_{-H}^H g_1^k \mathrm{d}y & \text{if Pe} \in (-2,2), \\ \int_{-H}^H g_2^k \mathrm{d}y & \text{if Pe} \notin (-2,2), \end{cases} \tag{26c}$$

$$g_1^k(y) = \sum_{i=2}^{n_x-1}\frac{u_y}{2}\left(c_{i+1,y}^k - c_{i-1,y}^k\right) + \frac{u_y}{2}\left[c_{2,y}^k + \frac{(-\varphi_{1/2} + u_y/2)c_{1,y}^k + q_W^k}{\varphi_{1/2} + u_y/2}\right]$$
$$+ \frac{u_y}{2}\left[\frac{q_E^k - (\varphi_{n_x+1/2} + u_y/2)c_{n_x,y}^k}{-\varphi_{n_x+1/2} + u_y/2} - c_{n_x-1,y}^k\right], \tag{26d}$$

$$g_2^k(y) = \sum_{i=2}^{n_x-1}\left[\xi_y\left(c_{i,y}^k - c_{i+1,y}^k\right) + \eta_y\left(c_{i,y}^k - c_{i-1,y}^k\right)\right]$$
$$+ \xi_y\left(c_{1,y}^k - c_{2,y}^k\right) + \eta_y\left(c_{n_x,y}^k - c_{n_x-1,y}^k\right)$$
$$- \frac{u_y c_{1,y}^k + q_W^k}{\varphi_{1/2} + \eta_y} - \frac{q_E^k - u_y c_{n_x,y}^k}{\varphi_{n_x+1/2} + \eta_y}, \tag{26e}$$

where $c_{i,y}^k = c(x_i, y, t_k)$ is the pore-scale concentration continuous in y, to be discretized by an appropriate quadrature rule in (26c); $\text{Pe} = u/d$; $u_y = u(y)$; $\xi_y = \max(-u_y, 0)$; $\eta_y = \max(u_y, 0)$; $\varphi_s = d_s/\mathcal{A}_s$ ($s = 1/2$ and $s = n_x + 1/2$); $d_{i+1/2} = \mathcal{D}\mathcal{A}_{i+1/2}/\Delta x_{i+1/2}$; $d_{i-1/2} = \mathcal{D}\mathcal{A}_{i-1/2}/\Delta x_{i-1/2}$ and $\mathcal{A}_{i+1/2}$ and $\mathcal{A}_{i-1/2}$ are the respective lengths of the eastern and western boundaries of the CV centered at x_i; and q_W and q_E are the unknown continuum-scale mass fluxes at the western and eastern internal boundaries separating the pore- and continuum-scale representations. They serve as boundary conditions for the pore-scale simulations in the $I^\star$-th CV. We stress that $RHS_{I^\star}$ is a function of pore-scale concentration and that the latter depends on q_W and q_E. An iterative algorithm to solve (24)–(26) is described below.

3.2. Hybrid algorithm

The solution of the coupled system (16)–(20) or its discretized form (24)–(26) reduces to finding zeros (q_E, q_W) of an algebraic system of equations in the form

$$F(q_E, q_W) = 0, \quad H(q_E, q_W) = 0, \tag{27}$$

where $q_E = q_{I^\star+1/2}$ and $q_W = q_{I^\star-1/2}$ are the unknown continuum-scale mass fluxes at the western and eastern edges of the $I^\star$-th cell. The hybrid pore-scale/continuum-scale algorithm can be formulated as follows.

(1) *Initialization.* At timestep T^N, c^N and $\bar{c}^N$ are known.
(2) *Guess for fluxes.* Make a guess for q_W and q_E, i.e., pick two constants. This imposes the Robin (or third type) conditions at the eastern and western boundaries of the pore-scale simulations domain:

$$\mathcal{D}\frac{\partial c}{\partial x} - uc = q_W, \quad x = X_{I^\star-1/2}, \quad y \in [-H, H], \tag{28a}$$

$$-\mathcal{D}\frac{\partial c}{\partial x} + uc = q_E, \quad x = X_{I^\star+1/2}, \quad y \in [-H, H]. \tag{28b}$$

The boundary conditions at the north and south boundaries (solid walls of the fracture) are defined by (16b).
(3) *Pore-scale evolution and source-term evaluation.* The pore-scale problem (16), supplemented with the boundary conditions (28) is evolved from T^N to T^{N+1}. The source term G at node $I^\star$ is evaluated from (26c)–(26e).
(4) *Continuum-scale evolution.* The continuum-scale concentration $\bar{c}$ is evolved from T^N to T^{N+1} by using the Thomas algorithm to solve the tri-diagonal system (24).
(5) *Continuum-scale fluxes computation.* Continuum-scale fluxes $\tilde{q}_W$ and $\tilde{q}_E$ at locations $X_{I^\star-1/2}$ and $X_{I^\star+1/2}$ are computed by means of (A.2) and compared with the q_W and q_E from step 2.

Table 1
Parameter values used in the simulations of reactive transport in a fracture. The dimensionless parameters are defined as $\text{Pe} = UL/\mathcal{D}, \text{Pe}_y = u_m H/\mathcal{D}, \text{Da} = KL/D, \text{Da}_y = \mathscr{K}H/\mathcal{D}, \text{Da}_{out} = K_{out}L/D, \text{Da}_{y,out} = \mathscr{K}_{out}H/\mathcal{D}$.

Parameters	Continuum-scale	Pore-scale
Domain length in x	$L = 20$ [L]	$\Delta X = 0.25$ [L]
Domain length in y	–	$2H = 0.25$ [L]
Nodes in x-direction	$N_X = 80$	$n_x = 30$
Nodes in y-direction	–	$n_y = 20$
Hybrid node	$I^\star = 15$	–
Time step	$\Delta T = 0.0005$ [T]	$\Delta t = 0.00001$ [T]
Diffusion coefficient	$D = 20.0015$ [L²/T]	$\mathcal{D} = 20$ [L²/T]
Kinematic viscosity	–	$v = 0.01$ [L²/T]
Case 1: Advection–diffusion		
Time domain	[0,0.4] [T]	[0,0.4] [T]
Maximum velocity	$U = 3.33$ [L/T]	$u_m = 5$ [L/T]
Reaction coefficient	$K = 0$ [1/T]	$\mathscr{K} = 0$ [L/T]
Péclet number	Pe ≈ 3.33	Pe$_y \approx 0.03$
Damköhler number	Da $= 0$	Da$_y = 0$
Case 2: Advection–reaction–diffusion (homogeneous $\mathscr{K}$)		
Time domain	[0,0.2] [T]	[0,0.2] [T]
Maximum velocity	$U = 10.0417$ [L/T]	$u_m = 15$ [L/T]
Reaction coefficient	$K = 39.55$ [1/T]	$\mathscr{K} = 5$ [L/T]
Péclet number	Pe ≈ 10	Pe$_y \approx 0.1$
Damköhler number	Da ≈ 40	Da$_y \approx 0.03$
Case 3: Advection–reaction–diffusion (heterogeneous $\mathscr{K}$)		
Time domain	[0,0.25] [T]	[0,0.25] [T]
Maximum velocity	$U = 10.0417$ [L/T]	$u_m = 15$ [L/T]
Reaction coefficient	$K_{out} = 39.55$ [1/T]	$\mathscr{K}_{out} = 5$ [L/T]
	$K_{in} = 225$ [1/T]	$\mathscr{K}_{in} = 450$ [L/T]
Péclet number	Pe ≈ 10	Pe$_y \approx 0.1$
Damköhler number	Da$_{out} \approx 40$	Da$_{y,out} = 0.03$
	Da ≈ 225	Da$_y = 2.8$

(6) *Convergence check and iteration.* Select an acceptable tolerance ϵ. If $|\tilde{q}_W - q_W| > \epsilon$ or $|\tilde{q}_E - q_E| > \epsilon$, use, e.g., the Broyden method, to refine the guess of q_W and q_E and go to step 2. If both $|\tilde{q}_W - q_W| \leqslant \epsilon$ and $|\tilde{q}_E - q_E| \leqslant \epsilon$, then the convergence is reached. March forward in time ($N := N + 1$) and go to step 1.

4. Numerical results

In Section 4.1, we use advective–diffusive transport (Taylor dispersion) in a fracture with uniform reaction rates. This setting admits an analytical solution and, hence, is used to analyze the accuracy of the hybrid algorithm relative to that of its continuum (upscaled) counterpart. In Section 4.2, the reaction coefficient is taken to be highly heterogeneous. For this situation, we compare the hybrid solution with both a solution of the upscaled equation (18) and an averaged solution of the fully two-dimensional problem ("pore-scale simulations").

4.1. Hybrid validation

We consider the macroscopic problem (18) subject to the initial and boundary conditions

$$\bar{c}(x,0) = 1, \quad \bar{c}(0,t) = 0, \quad \frac{\partial \bar{c}}{\partial x}(\infty, t) = 0. \tag{29}$$

Its unique solution is

$$\bar{c}(x,t) = e^{-Kt}\left(1 - \frac{1}{\sqrt{\pi}}e^{Ux/D}\int_{\frac{x+Ut}{2\sqrt{Dt}}}^{+\infty} e^{-\eta^2}\,d\eta + \frac{1}{\sqrt{\pi}}\int_{\frac{x-Ut}{2\sqrt{Dt}}}^{+\infty} e^{-\eta^2}\,d\eta\right). \tag{30}$$

This exact solution is used to verify the accuracy of both the hybrid algorithm and the numerical solutions of the continuum problem (18) for advective–diffusive transport (Case 1 in Table 1) and advective–diffusive-reactive transport with uniform reaction rates (Case 2 in Table 1). The set of parameters used in these simulations are summarized in Table 1. These values are typical for flow and trans-
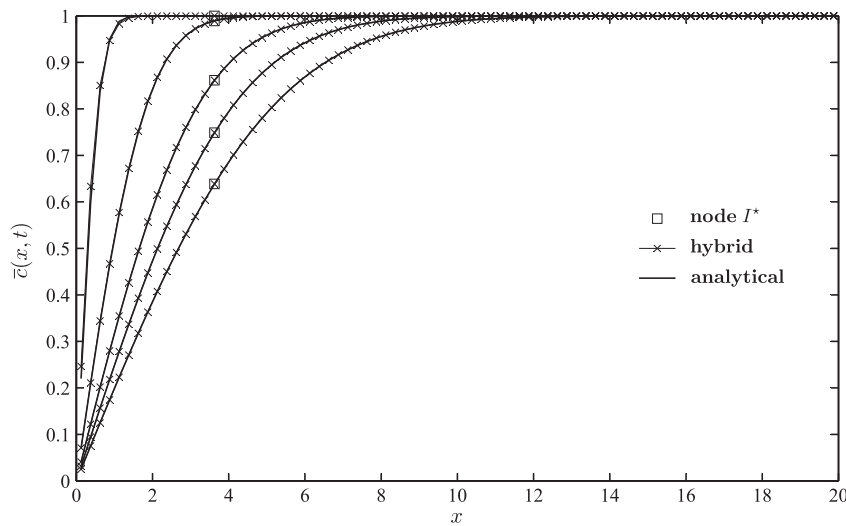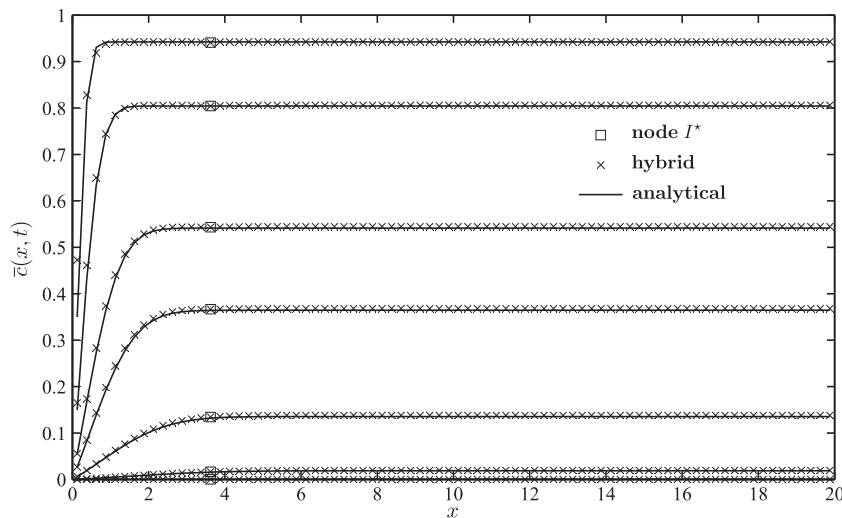

Fig. 4. Case 1 in Table 1: temporal snapshots of the average concentration $\bar{c}(x,t)$ computed with the analytical solution (30) (solid line) and hybrid simulations ($\times$) at times $t = 0.005$, $t = 0.05$, $t = 0.15$, $t = 0.25$, and $t = 0.395$ (from left to right). Symbol $\square$ indicates the location of node $I^\star$, where the pore- and continuum-scales are coupled.

Fig. 5. Case 2 in Table 1: temporal snapshots of the average concentration $\bar{c}(x,t)$ computed with the analytical solution (30) (solid line) and hybrid simulations ($\times$) at times $t = 0.001$, $t = 0.005$, $t = 0.015$, $t = 0.025$, $t = 0.05$, $t = 0.1$, and $t = 0.195$ (from top to bottom). Symbol $\square$ indicates the location of node $I^\star$, where the pore- and continuum-scales are coupled.
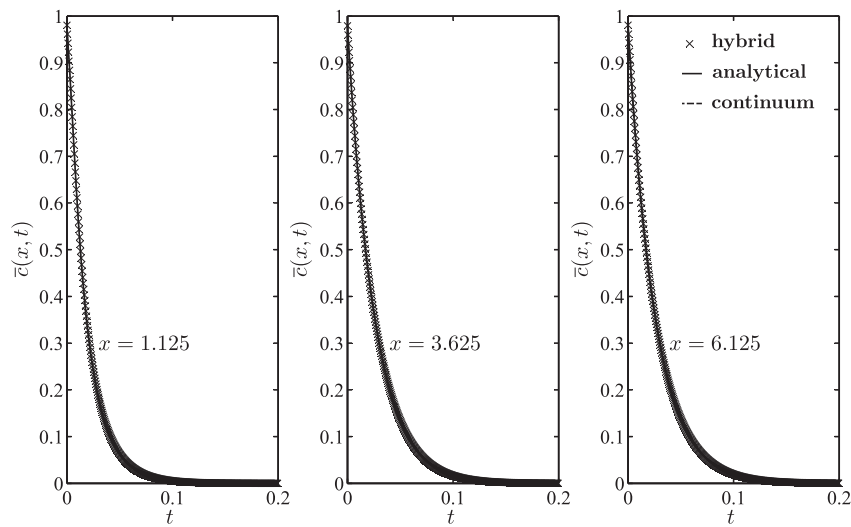
Fig. 6. Case 2 in Table 1: breakthrough curves at three locations, upstream and downstream of the hybrid node (figures on the left and on the right, respectively) and at the hybrid node $I^\star$ (center), computed with the analytical solution (30) (solid line), hybrid simulations ($\times$), and the numerical solution of the continuum model (18) (dashed line).
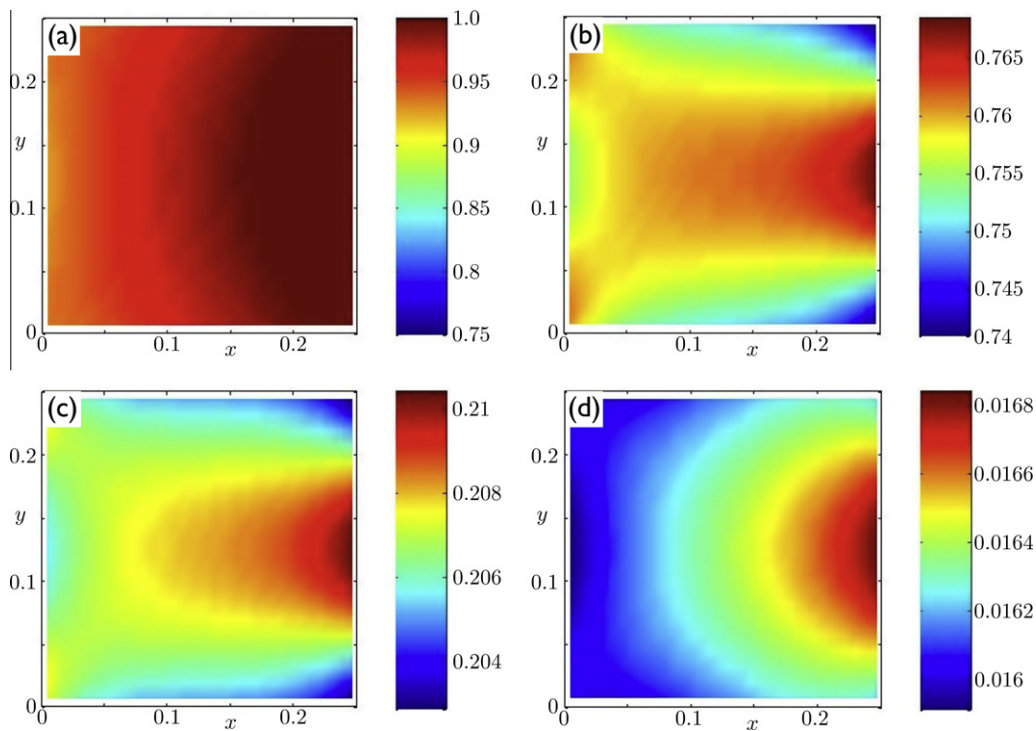

Fig. 7. Case 2 in Table 1: pore-sale concentration $c(x,y,t)$ in the hybrid node $I^\star$ at times $t = 0.0005$ (a), $t = 0.007$ (b), $t = 0.04$ (c), and $t = 0.1$ (d).

port processes through fractured media: experiments of transport in fractured media [10,11] with fracture aperture in the order of microns ($0.6 - 120$ μm) and weighted average velocity of 0.75 m/day have Péclet number in the range of $2.6 \times 10^{-3} - 0.52$.

Figs. 4–6 show a perfect agreement between the analytical and hybrid solutions. This is to be expected since all the necessary conditions for the validity of the macroscopic (averaged) transport Eq. (18) hold for the flow and transport regimes considered in Cases 1 and 2. The comparison between the numerical and analytical solutions of (18) also demonstrates that the choice of space–time discretization is adequate to ensure the required accuracy.

Hence, the discrepancy between the hybrid (and pore-scale) and continuum simulations observed in Section 4.2 is due to the breakdown of the latter rather than numerical errors.

Fig. 7 depicts the pore-scale concentration at the macro-scale node $I^\star$ at four temporal snapshots. The mass accumulation and mass depletion areas close to the boundaries arise from imposition of continuity of pore- and continuum-scale mass fluxes on the west and east edges of a continuum-scale element $I^\star$. Specifically, the continuum-scale mass fluxes q_E and q_W, which are constant along the respective edges of the $I^\star$-th CV, serve as uniform boundary conditions for the pore-scale simulations. However, the local
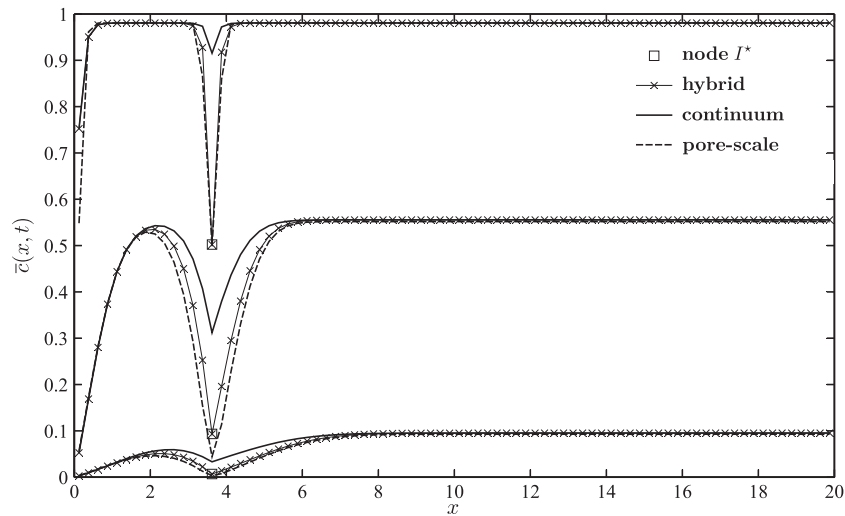
Fig. 8. Case 3 in Table 1: temporal snapshots of the average concentration $\bar{c}(x,t)$ computed with the 1D continuum model (18) (solid line), hybrid algorithm (×) and fully-resolved 2D pore-scale simulations (dashed line) at times $t = 0.0005$ (top), $t = 0.015$ (center) and $t = 0.06$ (bottom). Symbol □ indicates the location of node $I^\star$, where the pore- and continuum-scales are coupled.
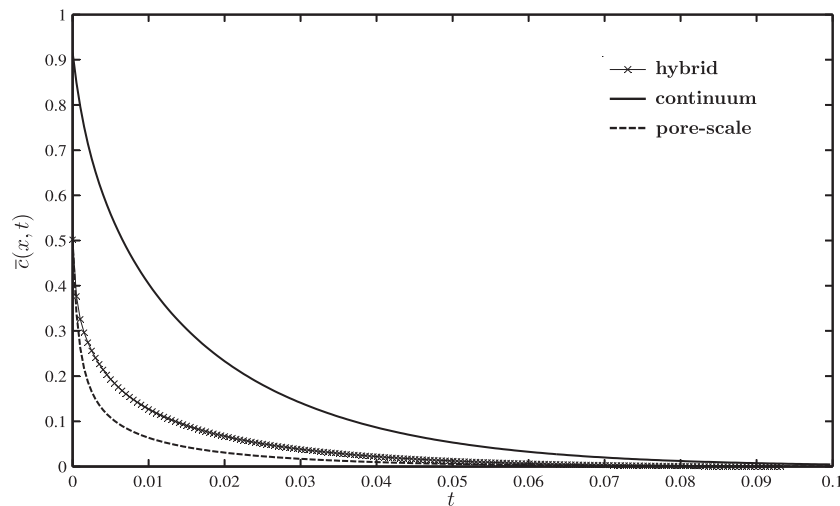

Fig. 9. Case 3 in Table 1: breakthrough curves at the hybrid node $I^\star$ computed with the 1D continuum model (18) (solid line), hybrid simulations (×), and fully-resolved 2D pore-scale simulations (dashed line).

distortions of the concentration distribution have a relatively little effect on the average (continuum-scale) concentration (see Figs. 5 and 6).

4.2. Hybrid simulations for highly localized heterogeneous reactions

In the last example we investigate the effects of heterogeneity in reaction rates. Specifically, we assume $\mathscr{K}$ at the $I^\star$-th node to be two orders of magnitude bigger than in the rest of the channel, with the Damköhler number Da_y changing from 0.03 to 2.8. Eq. (18) fails for $Da_y \geqslant 3$ as the effective reaction coefficient K changes sign for increasing positive values of $\mathscr{K}$ (i.e., increasing mass loss at the solid–liquid interface): this leads to the unphysical behavior of $K < 0$ (i.e., source) while mass is absorbed (degraded, etc.) at the micro-scale (i.e., sink).

While one can expect quantitative and qualitative differences between the upscaled model (18) and a fully 2D pore-scale solution for $Da_y \geqslant 3$, we show here that significant deviations from

the "exact" pore-scale solution occur even for $Da_y < 3$. This is done by comparing the results of our hybrid simulations with those obtained alternatively by solving the 1D continuum-scale Eq. (18) or by averaging the fully 2D pore-scale solution. Figs. 8 and 9 show respectively the continuum-scale concentration and breakthrough curves obtained from the upscaled 1D continuum-scale, hybrid and fully 2D pore-scale equations. At the location of high heterogeneity (see Fig. 8), the continuum-scale equation significantly overestimates the concentration, while the hybrid simulations improves

Table 2
Relative errors, $\mathscr{E} = 100\%|c_{ex} - c_{ap}|/c_{ex}$, between the "exact" fully-resolved pore-scale simulations (c_{ex}) and its approximate counterpart (c_{ap}) computed with either the continuum model or the hybrid simulations at the hybrid node $I^\star$.

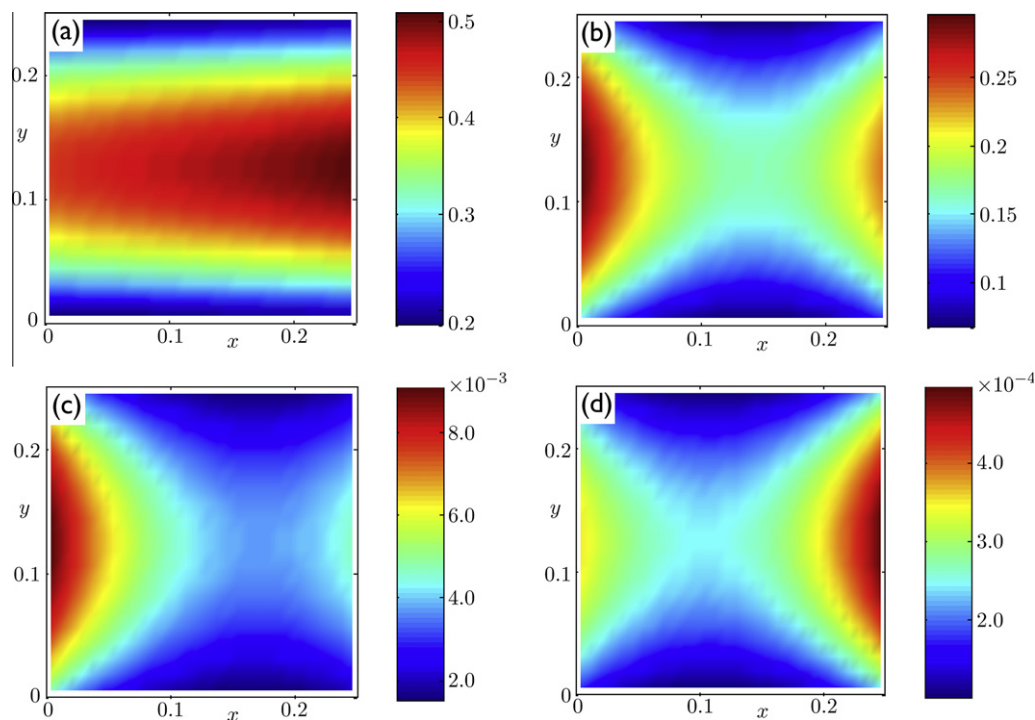|	$t = 0.0005$	$t = 0.015$	$t = 0.06$
Continuum model	200.8%	602.2%	890.7%
Hybrid algorithm	0.85%	110%	105%

Fig. 10. Case 3 in Table 1: pore-sale concentration $c(x,y,t)$ in the hybrid node $I^\star$ at times $t = 0.0005$ (a), $t = 0.0025$ (b), $t = 0.06$ (c), and $t = 0.15$ (d).

the prediction's accuracy (Table 2) at a fraction of computational cost. In our simulations conducted on a single-processor computer, the computational costs of the hybrid and fully-resolved 2D pore-scale simulations were 1.02×10^3 and 1.65×10^4 times larger than those of the 1D continuum-scale model (CPU time = 1.25).

The accuracy of the hybrid algorithm can be improved by enlarging Ω_p, the portion of the computational domain where the pore-scale simulations are carried out. When Ω_p becomes large enough to absorb the effects of the spike in the reaction rate constant, the hybrid algorithm's performance becomes similar to that shown in Figs. 5 and 6. Any improvement in accuracy comes at the expense of increased computational burden, since the pore-scale simulations have to be conducted in a larger region.

Fig. 8 reveals that pore-scale effects propagate from the domain of pore-scale simulations (CV $I^\star$) into the adjacent regions of continuum-scale simulations (e.g., CVs $I^\star - 1$ and $I^\star + 1$). This phenomenon is due to both a two-way coupling between the scales and the nonlinearity of reactive transport equations. The propagation of noise (unresolved fluctuations) from a fine-algorithm region into a coarse-algorithm region is a salient feature of hybrid simulations, occurring even in linear systems [1–3].

Fig. 10 depicts the concentration profile at the pore-scale at four different times and shows how the highly reacting walls produce strong concentration gradients between areas where mass is more quickly depleted because of fast reactions (close to the walls) relative to others where the major transport mechanism is diffusion (in the center of the channel).

5. Summary and conclusions

We developed a general algorithm to incorporate pore-scale (subgrid) effects into continuum models of reactive transport in porous and fractured media. Unlike multiscale methods that are based on empirical closures and/or approximations, our approach does not require prior knowledge about the macroscopic behavior of pore-scale variables. This is attained by treating the normal

fluxes through the internal boundaries separating the two formulations as unknown quantities. Given the intrinsic nonlinearity of such a formulation, the solution is found through an iterative procedure.

We applied our algorithm to model transport in a fracture with chemically reactive walls. A finite-volume implementation of the hybrid formulation was compared with corresponding analytical solutions, when available, and/or with "pore-scale" simulations of two-dimensional transport inside the fracture.

Our study leads to the following major conclusions:

- The proposed hybrid algorithm enables one to determine pore- and continuum-scale concentrations and fluxes in regions of a computational domain where advection–reaction–diffusion equations break down.
- The proposed method is capable of handling highly localized heterogeneities, provides a considerable improvement in accuracy, and enables one to properly capture the pore-scale physics.
- The hybrid formulation does not require additional parameters besides continuum properties of the porous media, physical and (bio)geochemical properties of a solute and fluid, and pore-scale geometry.
- The hybrid model formulation reduces to a zero-finding algorithm for a vector function. Such a formulation suggests its high adaptability to a wide variety of problems and different numerical schemes.
- Although not pursued here, the general hybrid formulation presented in Section 2.3 is suitable for implementation in commercial numerical codes.

A root-finding method used to couple the pore- and continuum-scale simulations determines the convergence and computational burden of the hybrid algorithm. While flexible, the Broyden method used in the present implementation of the hybrid algorithm might not be optimal in terms of either convergence or computational efficiency. Further research is needed in order to improve

the hybrid's computational efficiency and to relate the size of pore-scale simulation domain to the hybrid's accuracy.

Further generalizations to transport in porous media with complex pore-scale geometries will be addressed in future research together with full resolution of flow equation at the pore scale, the removal of the overlap between the two regions, and the possibility of incorporating uncertain pore geometry.

Acknowledgments

Appendix A

A.1. Discrete form of (18) for nodes other than $I^\star$

Integration of (18) over a CV centered at X_I gives

$$\frac{\partial \bar{c}_I}{\partial T}\Delta X_I + (U\bar{c})_{I+1/2} - (U\bar{c})_{I-1/2} = \mathcal{D}_{I+1/2}(\bar{c}_{I+1} - \bar{c}_I)$$
$$- \mathcal{D}_{I-1/2}(\bar{c}_I - \bar{c}_{I-1}) - K\bar{c}_I\Delta X_I, \qquad (A.1)$$

where $\mathcal{D}_s = D/\Delta X_s$ with $s = I - 1/2$ and $I + 1/2$.

The total fluxes through the western and eastern faces of the CV centered at X_I are [23]

$$q_{I-1/2} = (U\bar{c})_{I-1/2} - \mathcal{D}_{I-1/2}(\bar{c}_I - \bar{c}_{I-1}), \qquad (A.2a)$$
$$q_{I+1/2} = (U\bar{c})_{I+1/2} - \mathcal{D}_{I+1/2}(\bar{c}_{I+1} - \bar{c}_I), \qquad (A.2b)$$

respectively. Concentrations $\bar{c}_{I+1/2}$ and $\bar{c}_{I-1/2}$ have to be determined in function of $\bar{c}_I, \bar{c}_{I-1}$ and $\bar{c}_{I+1}$. Combining (A.1) and (A.2) and integrating over the macroscopic time step $[T_N, T_{N+1}]$, we obtain

$$(\bar{c}_I^{N+1} - \bar{c}_I^N)\frac{\Delta X_I}{\Delta T} = \theta(q_{I-1/2}^{N+1} - q_{I+1/2}^{N+1} - K\bar{c}_I^{N+1}\Delta X_I)$$
$$+ (1-\theta)(q_{I-1/2}^N - q_{I+1/2}^N - K\bar{c}_I^N\Delta X_I), \qquad (A.3)$$

where $\theta \in [0,1]$. Setting $\theta = 0$, $\theta = 1/2$, or $\theta = 1$ results in an explicit, Cranck–Nicolson, or fully implicit scheme, respectively. The fluxes are evaluated by means of the hybrid differencing scheme [19], based on a combination of a central (second order accurate) and an upwind (first order accurate) differencing scheme. Accordingly,

$$q_{I-1/2} = \frac{U_{I-1/2}}{2}\left[\left(1 + \frac{2}{\hat{\mathrm{Pe}}_{I-1/2}}\right)\bar{c}_{I-1} + \left(1 - \frac{2}{\hat{\mathrm{Pe}}_{I-1/2}}\right)\bar{c}_I\right], \qquad (A.4a)$$

$$q_{I+1/2} = \frac{U_{I+1/2}}{2}\left[\left(1 - \frac{2}{\hat{\mathrm{Pe}}_{I+1/2}}\right)\bar{c}_{I+1} + \left(1 + \frac{2}{\hat{\mathrm{Pe}}_{I+1/2}}\right)\bar{c}_I\right], \qquad (A.4b)$$

$$\text{where} \quad \hat{\mathrm{Pe}}_i = \begin{cases} \mathrm{Pe}_i, & \mathrm{Pe}_i \in (-2,2), \\ 2, & \mathrm{Pe}_i \geqslant 2, \\ -2, & \mathrm{Pe}_i \leqslant -2, \end{cases} \qquad (A.5)$$

$i = I - 1/2$ and $I + 1/2$, and $\mathrm{Pe}_i = U_i/\mathcal{D}_i$. Combination of (A.3) and (A.4) with the fully implicit time integration scheme ($\theta = 1$) leads to (24), where

$$A_{I-1} = -a_{I-1}, \quad A_I = \frac{\Delta X_I}{\Delta T} + \bar{a}_I, \quad A_{I+1} = -a_{I+1}, \quad a_0 = 0, \qquad (A.6a)$$

$$a_{I+1} = \max\left(-U_{I+1/2}, \mathcal{D}_{I+1/2} - \frac{U_{I+1/2}}{2}, 0\right), \quad \mathcal{D}_{I+1/2} = \frac{D}{\Delta X_{I+1/2}}, \qquad (A.6b)$$

$$a_{I-1} = \max\left(-U_{I-1/2}, \mathcal{D}_{I-1/2} + \frac{U_{I-1/2}}{2}, 0\right), \quad \mathcal{D}_{I-1/2} = \frac{D}{\Delta X_{I-1/2}}, \qquad (A.6c)$$

$$a_{N_x} = 0, \quad \bar{a}_I = a_{I-1} + a_{I+1} + (U_{I+1/2} - U_{I-1/2}) + K\Delta X_I - \bar{S}_I, \qquad (A.6d)$$

$$\mathrm{RHS}_I^N = \frac{\Delta X_I}{\Delta T}\bar{c}_I^N + \widetilde{S}_I \qquad (A.6e)$$

and $\widetilde{S}_I$ and $\bar{S}_I$ are determined by numerical discretization of boundary conditions at the macroscale. For uniform velocity U, we obtain (25).

A.2. Discrete form of (19) in node $I^\star$

Integrating (19) over the macroscopic CV centered at node $I^\star$ and over a macroscale time step, and using the implicit time integration scheme ($\theta = 1$), gives

$$\frac{\Delta X_{I^\star}}{\Delta T}\left(\bar{c}_{I^\star}^{N+1} - \bar{c}_{I^\star}^N\right) = d_{I^\star+1/2}\left(\bar{c}_{I^\star+1}^{N+1} - \bar{c}_{I^\star}^{N+1}\right) - d_{I^\star-1/2}\left(\bar{c}_{I^\star}^{N+1} - \bar{c}_{I^\star-1}^{N+1}\right)$$
$$\frac{\Delta t}{\Delta T}\sum_{k=1}^{n_t}\left[\sum_{i=1}^{n_x}\int_{x_{i-1/2}}^{x_{i+1/2}}g(x)\mathrm{d}x\right]^{k+1}, \qquad (A.7)$$

where

$$g(x) = -\frac{\mathscr{K}}{2H}[c(x,y=H) + c(x,y=-H)] - \frac{1}{2H}\int_{-H}^H u(y)\frac{\partial c}{\partial x}\mathrm{d}y. \qquad (A.8)$$

Using a numerical quadrature for the spatial integral in (A.7) yields

$$\frac{\Delta t}{\Delta T}\sum_{k=1}^{n_t}\sum_{i=1}^{n_x}\Delta x_i[g(x_i)]^{k+1} = \frac{1}{2HN_T}\sum_{k=1}^{n_t}\sum_{i=1}^{n_x}\Delta x_i\Big[-\mathscr{K}\left(c_{i,H} + c_{i,-H}\right)$$
$$- \int_{-H}^H u(y)\frac{c_{i+1/2,y} - c_{i-1/2,y}}{\Delta x_i}\mathrm{d}y\Big]^{k+1}. \qquad (A.9)$$

If $\mathrm{Pe} \in (-2,2)$, then $c_{i+1/2}$ and $c_{i-1/2}$ ($i = 2,\ldots,n_x - 1$) can be approximated by

$$c_{i-1/2} = \frac{c_{i-1} + c_i}{2}, \quad c_{i+1/2} = \frac{c_i + c_{i+1}}{2}. \qquad (A.10)$$

At the internal boundaries separating the continuum- and pore-scale domains, $c_{1/2}$ (i.e., $i = 1$) and $c_{n_x+1/2}$ (i.e., $i = n_x$) must satisfy boundary conditions (28a) and (28b), respectively. This leads to

$$c_{1/2} = \frac{\mathcal{A}_{1/2}q_W + (-d_{1/2} + \mathcal{A}_{1/2}U/2)c_1}{-\mathcal{A}_{1/2}U/2 - d_{1/2}}, \qquad (A.11a)$$

$$c_{n_x+1/2} = \frac{\mathcal{A}_{n_x+1/2}q_E - (d_{n_x+1/2} + \mathcal{A}_{1/2}U/2)c_{n_x}}{\mathcal{A}_{1/2}U/2 - d_{n_x+1/2}}. \qquad (A.11b)$$

Combining (A.7) with (A.9)–(A.11) yields (26d).

If $\mathrm{Pe} \leqslant -2$ or $\mathrm{Pe} \geqslant 2$, then $c_{i+1/2}$ and $c_{i-1/2}$ ($i = 2,\ldots,n_x - 1$) can be approximated by

$$c_{i-1/2} = \eta_{i-1/2}c_{i-1} - \xi_{i-1/2}c_i, \quad c_{i+1/2} = \eta_{i+1/2}c_i - \xi_{i+1/2}c_{i+1}, \qquad (A.12)$$

where $\xi = \max\{-u,0\}$ and $\eta = \max\{u,0\}$. For $i = 1$ and $i = n_x$, the following formulae hold

$$c_{1/2} = \frac{\mathcal{A}_{1/2}q_W - c_1(d_{1/2} + \mathcal{A}_{1/2}\xi_{1/2})}{-d_{1/2} - \mathcal{A}_{1/2}\eta_{1/2}}, \qquad (A.13a)$$

$$c_{n_x+1/2} = \frac{\mathcal{A}_{n_x+1/2}q_E - c_{n_x}(d_{n_x+1/2} + \mathcal{A}_{n_x+1/2}\eta_{n_x+1/2})}{-d_{n_x+1/2} - \mathcal{A}_{1/2}\xi_{n_x+1/2}}. \qquad (A.13b)$$

Combining (A.7) with A.9, A.12, and (A.13) leads to (26e).

References

[1] Alexander FJ, Garcia AL, Tartakovsky DM. Algorithm refinement for stochastic partial differential equations: 1. Linear diffusion. J Comput Phys 2002;182:47–66.
[2] Alexander FJ, Garcia AL, Tartakovsky DM. Algorithm refinement for stochastic partial differential equations: II. Correlated systems. J Comput Phys 2005;207(2):769–87.
[3] Alexander FJ, Garcia AL, Tartakovsky DM. Noise in algorithm refinement methods. Comput Sci Eng 2005;7(3):32–8.

[4] Auriault J, Adler PM. Taylor dispersion in porous media: analysis by multiple scale expansions. Adv Water Resour 1995;4(18):217–26.

[5] Battiato I, Tartakovsky DM. Applicability regimes for macroscopic models of reactive transport in porous media. J Contam Hydrol 2011;120-121:18–26. doi:10.1016/j.jconhyd.2010.05.005.

[6] Battiato I, Tartakovsky DM, Tartakovsky AM, Scheibe T. On breakdown of macroscopic models of mixing-controlled heterogeneous reactions in porous media. Adv Water Resour 2009;32:1664–73. doi:10.1016/j.advwatres.2009.08.008.

[7] Christie MA. Upscaling for reservoir simulation. J Petrol Technol 1996;48:1004–10.

[8] de Marsily G. Quantitative hydrogeology. San Diego, California: Academic Press; 1986.

[9] Efendief Y, Durlofsky LJ. A generalized convection–diffusion model for subgrid transport in porous media. Multiscale Model Simulat 2003;1(3):504–26.

[10] Grisak GE, Pickens JF. Solute transport through fractured media, 1. The effect of matrix diffusion. Water Resour Res 1980;16(4):719–30.

[11] Grisak GE, Pickens JF, Cherry JA. Solute transport through fractured media, 2. Column study of fractured till. Water Resour Res 1980;16(4):731–9.

[12] Hesse F, Radu FA, Thullner M, Attinger S. Upscaling of the advection–diffusion–reaction equation with Monod reaction. Adv Water Resour 2009;32:1336–51. doi:10.1016/j.advwatres.2009.05.009.

[13] Langlo P, Espedal MS. Macrodispersion for two-phase, immiscible flow in porous media. Adv Water Resour 1994;17:297–316.

[14] Leemput P, Vandekerckhove C, Vanroose W, Roose D. Accuracy of hybrid lattice Boltzmann/finite difference schemes for reaction diffusion systems. Multiscale Model Simulat 2007;6(3):838–57.

[15] Meakin P, Tartakovsky AM. Modeling and simulation of pore-scale multiphase fluid flow and reactive transport in fractured and porous media. Rev Geophys 2009;47:RG3002. doi:10.1029/2008RG000263.

[16] Mikelic A, Devigne V, Van Duijn CJ. Rigorous upscaling of the reactive flow through a pore, under dominant Péclet and Damköhler numbers. SIAM J Math Anal 2006;38(4):1262–87.

[17] Neuman SP, Tartakovsky DM. Perspective on theories of anomalous transport in heterogeneous media. Adv Water Resour 2009;32(5):670–80.

[18] Smolarkiewicz PK, Winter CL. Pores resolving simulation of Darcy flows. J Comput Phys 2010;229(9):3121–33.

[19] Spalding DB. A novel finite-difference formulation for differential expressions involving both first and second derivatives. Int J Numer Methods Eng 1972;4:551–9.

[20] Sukop MC, Thorne DT. Lattice Boltzmann modeling: an introduction for geoscientists and engineers. New York: Springer; 2005.

[21] Tartakovsky AM, Tartakovsky DM, Meakin P. Stochastic Langevin model for flow and transport in porous media. Phys Rev Lett 2008;101: 044502.

[22] Tartakovsky AM, Tartakovsky DM, Scheibe TD, Meakin P. Hybrid simulations of reaction-diffusion systems in porous media. SIAM J Sci Comput 2008;30(6):2799–816.

[23] Versteeg HK, Malalasekera M. An introduction to computational fluid dynamics: the finite volume method. Harlow, England: Pearson Education Ltd. 2007.

[24] Wood BD, Radakovich K, Golfier F. Effective reaction at a fluid–solid interface: applications to biotransformation in porous media. Adv Water Resour 2007;30(6–7):1630–47.